Mechatronics 78 (2021) 102598

Contents lists available at ScienceDirect

Mechatronics

journal homepage: www.elsevier.com/locate/mechatronics

Modulation of control authority in adaptive haptic shared control paradigms☆

Vahid Izadi *, Amir H. Ghasemi

Department of Mechanical Engineering and Engineering Science, University of North Carolina Charlotte, Charlotte, NC, 28223, United States of America

ARTICLE INFO

Keywords:
Adaptive haptic shared control
Human–automation interaction
Nonlinear model predictive control
Continuation/GMRES solver
Arbitration of the control authority

ABSTRACT

This paper presents an adaptive haptic shared control framework wherein a driver and an automation system are physically connected through a motorized steering wheel. An adaptive impedance controller for the automation system is introduced to enable the automation system to dynamically and smoothly exchange the control authority with the human partner. To determine an optimal modulation policy, a cost function is considered, and its terms are defined to minimize the performance error and reduce the disagreement between the human and automation system. We employed a nonlinear stochastic model predictive approach to solve the cost function subjected to probabilistic uncertainties in human's biomechanics. The polynomial chaos expansions are employed to obtain a computationally tractable form of the cost function, and the continuation generalized minimum residual method is utilized to solve the tractable nonlinear cost function. To demonstrate the effectiveness of the proposed approach, we consider a scenario where the human and the automation system both detect an obstacle and negotiate on controlling the steering wheel so that the obstacle can be avoided safely. For this scenario, four interaction modes are defined based on the cooperation status (cooperative and uncooperative) and the control transfer's desired direction (human to automation or automation to human). The numerical results demonstrate that when the human's control command is sufficient for avoiding the obstacle, by modulating and adopting smaller values for the impedance controller, the disagreement between the human and automation systems can be reduced. On the other hand, when the human's control command is insufficient, by modulating and adopting larger values for the impedance controller parameters, the automation system gains the control authority and ensures the safety of the obstacle avoidance task. Additionally, we performed a set of tests with processors in the loop (PIL) to show the proposed predictive controller can compute the optimal modulation policy in real-time. Using two low-cost micro-controllers, the PIL results show high computational speed and numerical accuracy for the proposed method.

1. Introduction

Haptic Shared Control is a shared control paradigm wherein humans interact with co-robot through a physical object [1,2]. Haptic shared control paradigms have a wide range of applications, from transformative technologies in which a fully autonomous system is not yet accessible/feasible (e.g., service robots, semi-autonomous vehicles, smart manufacturing) to applications where human–robot interactions are inevitable or even desirable (e.g., rehabilitative devices, care robots, and educational robots) [1–11]. In a haptic shared control paradigm, both humans and co-robots can simultaneously exert their control inputs, and by virtue of haptic feedback continuously, monitors each other's actions. With recent advances in artificial intelligence and robotics, conflicts may arise in which an automation system can make decisions different from the human partner's. For instance, in steering a vehicle, there might be cases where both humans and automation detect an obstacle but select different trajectories to avoid it [2].

While human teams can be exceptionally efficient at resolving conflicts using shared mental models, the ability of co-robots for negotiating and resolving conflicts is significantly underdeveloped. To enable a co-robot to resolve a conflict, a series of challenges shall be addressed. First, a model that can capture the human's intent shall be developed [12–16]. Second, algorithms that can identify the current interaction mode shall be developed [17–21]. Third, algorithms that support arbitration of control authority shall be created [22–25]. Finally, interfaces that allows bi-directional communication between the human and co-robot shall be made [26–30].

This paper's focuses on the third technical challenge. In particular, we consider the co-robot with a similar structure to the human partner

☆ This paper was recommended for publication by Associate Editor Lianqing Liu.

* Corresponding author.
E-mail address: vizadi@uncc.edu (V. Izadi).

https://doi.org/10.1016/j.mechatronics.2021.102598
Received 15 January 2021; Received in revised form 29 April 2021; Accepted 6 June 2021
Available online 9 July 2021

with a two-level hierarchical control structure. The higher-level controller generates the co-robot desired reference (intent), determines the current interaction mode, and estimates the human's intent. The lower level is an impedance controller generating the required torque signals. In this paper, we focus on the design of this lower-level controller. While the fundamental approaches and models proposed in this research can be applied to a wide range of physical human–robot systems, we select semi-automated vehicles' steering control as a setup for exploring the proposed study. We consider a scenario where the human and the automation system detect an obstacle and negotiate on controlling the steering wheel so that the obstacle can be avoided safely. To this end, the simulations involve four interaction modes addressing the cooperation status (cooperative and uncooperative) and the desired direction of the control transfer (active safety and assistive).

To determine how the automation system's impedance controller parameters should be dynamically modulated so that a smooth transition of control authority can occur, a cost function is designed to maximize task performance and minimize the disagreement between the human and the co-robot. We utilize a stochastic nonlinear model-predictive control approach to solve the optimal control problem. To obtain a tractable form of the cost function, the generalized polynomial chaos (PC) scheme is utilized to formulate the deterministic surrogate of the stochastic MPC with probabilistic constraints. In the PC method, the implicit mappings among the uncertain parameters (i.e., human arm's biomechanics) and the states are replaced with explicit functions in the form of a sequence of orthogonal polynomials, whose coefficient can be calculated from the expansion coefficients [31,32]. We then employed the continuation generalized minimum residual (C/GMRES) solver that provides an iterative algorithm to solve the tractable nonlinear model predictive controller [33–36]. In this method, first, the optimal control problem is discretized over the horizon. A differential equation is then obtained by using the continuation method to update the sequence of control inputs [36]. Since the differential equation involves a large linear equation, the GMRES method [37] is employed to solve the linear equation. It is shown that the C/GMRES requires much less computational expenses than other iterative methods such as Newton's method. Moreover, C/GMRES involves no line search, which is also significantly different from standard optimization methods [38]. To evaluate the proposed methods' computational complexity, a set of PIL tests are conducted using two low-cost microcontrollers (STM32F4and ATmega2560). These processors provide direct access to the CPU's hardware resources to implement the proposed algorithm without involving the time management for handling the serial port for the data communication between the target board and the host computer. The comparative studies in the real-time PIL testbed show high accuracy with appropriate computation time in the STM32F4 Discovery target board.

In summary, the contributions of this paper are (*i*) development of a model for a haptic shared control paradigm wherein the topic of role negotiation, role allocation, and intention integration can be systematically explored in two levels of mind (intent/decision making) and motor (human biomechanics/robot's impedance control); (*ii*) development of a set of stochastic optimal control algorithms for modulating the automation's impedance controller parameters so that the control authority can dynamically be arbitrated between the human and automation systems; (*iii*) validation of the optimal controller for real-time implementation using a series of process-in-the-loop tests.

The outline of this paper is as follows. In Section 2, we model the adaptive haptic shared control paradigm, and the equations of motions are derived. In Section 3, the problem of modulation of control authority is presented as an optimal control problem. To demonstrate the proposed approach's effectiveness, a set of numerical simulations are illustrated in Section 4. The PIL results on the low-cost microcontrollers are presented in Section 5, which shows the proposed method's implementation ability in real-time execution. Section 6 consists of the conclusions and the future directions for this research.

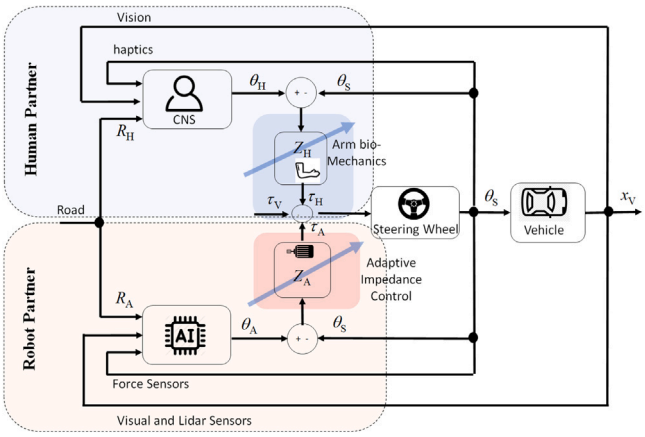

Fig. 1. A general model of control sharing between driver and automation.

2. Adaptive haptic shared control framework

Fig. 1 shows a schematic of an adaptive haptic shared control paradigm. Three entities each impose a torque on the steering wheel: a driver through his hands, an automation system through a motor, and the road through the steering linkage.

We model the human and automation system with a similar structure. In particular, we model the driver as a hierarchical two-level controller. The upper-level control represents the cognitive controller, and its output, θ_H, represents the driver's intent. The lower-level represent the human's biomechanics, Z_H, and is considered back-drivable [6]. To indicate that driver's biomechanic parameters vary with changes in grip on the steering wheel, use of one hand or two, muscle co-contraction, or posture changes, we have drawn an arrow through human Z_H.

Similarly, the automation system is modeled as a higher-level controller (AI) coupled with a lower-level impedance controller. The automation system is also considered to be back-drivable, and the gains of the impedance controller, Z_A, are designed to be modest rather than infinite. In other words, the automation is not intended to behave as an ideal torque source; instead, the automation imposes its command torque τ_A through an impedance Z_A that is approximately matched to the human impedance Z_H.

Furthermore, the reference signals R_H and R_A represent the goals of the driver and the automation system, respectively. It should be noted that these goals may not necessarily be the same, which is when the negotiation of control authority becomes essential. To generate algorithms that support the negotiation and dynamic transfer of the control authority between the human and co-robot, the robot can adjust its behavior at a higher level (changing intent) as well as at the lower level (changing Z_A). Specifically, from the model presented in Fig. 1, it follows that the steering angle θ_S is not only a function of the human's intent θ_H, automation's intent θ_A, and the road feedback torque τ_V, but also its a function of human arm's biomechanics Z_H as well as the gains of the impedance controller Z_A [39]. The crux of this paper lies in the design of a back-drivable impedance Z_A such that it enhances the negotiation and transfer of control authority between the human and automation system. To this end, we present the equations of motion of the lower-level of the adaptive haptic shared control framework shown in Fig. 2.

2.1. Equations of motion

Fig. 2-A shows a free body diagram of an adaptive haptic shared control paradigm consisting of a driver, a steering wheel, a steering shaft, and an automation system. Fig. 2-A demonstrates a simplified model of a driver arms' bio-mechanics in the form of a mass–spring–damper system connected to a motion source representing the driver's

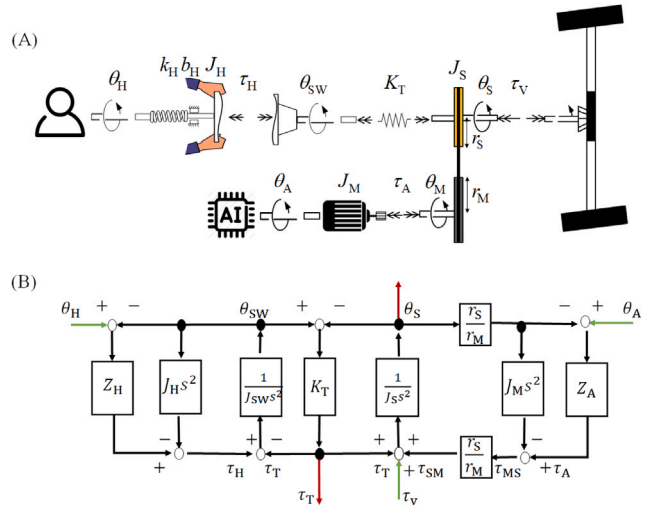

Fig. 2. (A) Free body diagram of a haptic shared steering control, (B) A block diagram is laid out to highlight the interaction ports between subsystems. [6].

intent, θ_H. The steering wheel is modeled as a disk with a rotational inertia of J_{SW}. A differential torque sensor is modeled as a rotational spring with stiffness K_T and connected to the steering wheel and steering shaft. The steering shaft is also considered as a rotational bar with the inertia of J_S that is connected to the steering wheel on the left side, to the rack and pinion on the right side, and the automation system through a timing belt with a mechanical advantage of r_S/r_M. The block diagram of the lower-level of the adaptive haptic shared control is also shown in Fig. 2-B. In this block diagram, signals of θ_H, θ_A, and τ_V are considered as exogenous signals; signals of differential torque τ_T and the steering shaft angle θ_S can be measured by the on-board sensors.

It follows from Fig. 2 that the equations of motion for the steering wheel, steering column and the motor can be expressed as

$$J_{SW}\ddot{\theta}_{SW} = \tau_H - \tau_T \tag{1a}$$

$$J_S\ddot{\theta}_S = \tau_T + \tau_V + \tau_{SM} \tag{1b}$$

$$J_M\ddot{\theta}_M = \tau_A - \tau_{MS} \tag{1c}$$

where τ_{SM} and τ_{MS} represent the internal torque imposed by the timing belt. It should be noted that the kinematic and kinetic constraints imposed by the timing belt are $r_M\theta_M = r_S\theta_S$ and $r_M\tau_{SM} = r_S\tau_{MS}$.

Modeling the driver as a spring–mass–damper with a proximal motion source $\theta_H(t)$, the torque applied by the human is [8]

$$\tau_H = -J_H\ddot{\theta}_{SW} + B_H(\dot{\theta}_H - \dot{\theta}_{SW}) + K_H(\theta_H - \theta_{SW}) \tag{2a}$$

where J_H, B_H, and K_H are the inertia, damping and stiffness of the driver's arm. Similarly, considering an impedance controller in the lower-level of the automation system, the toque generated by the motor can be presented as

$$\begin{aligned}\tau_A &= B_A(\dot{\theta}_A - \dot{\theta}_M) + K_A(\theta_A - \theta_M)\\ &= B_A(\dot{\theta}_A - \frac{r_S}{r_M}\dot{\theta}_s) + K_A(\theta_A - \frac{r_S}{r_M}\theta_S)\end{aligned} \tag{2b}$$

where K_A, B_A represent the gains of the impedance controller. Furthermore, it follows from Fig. 2 that the torque measured by the torque sensor can be expressed as

$$\tau_T = K_T(\theta_{SW} - \theta_S) \tag{2c}$$

It follows from Eq. (2a) that human's torque is not only a function of human's intent θ_H but also the biomechanic parameters Z_H. By modulating these parameters, the human can either yield or retain the control authority. Similarly, algorithms can be developed to give the automation the ability to either yield authority or retain authority as a function of driver behavior and sensed threats to safety. To present how human's bio-mechanics and the automation's impedance controller parameters may evolve in time, we introduce the following simple but generic dynamic models as

$$\dot{Z}_H(t) = \alpha_H Z_H(t) + \beta_H \Gamma_H(t) + \varrho(t) \tag{3a}$$

$$\dot{Z}_A(t) = \alpha_A Z_A(t) + \beta_A \Gamma_A(t) \tag{3b}$$

where $Z_H = [B_H\ K_H]^T$, $Z_A = [B_A\ K_A]^T$, and $\Gamma_H = [\Gamma_{bH}(t)\ \Gamma_{kH}(t)]^T$ is the human's control action for modulating his impedance Z_H, $\Gamma_A = [\Gamma_{bA}(t)\ \Gamma_{kA}(t)]^T$ is the automation's control input for modulating its impedance Z_A, and $\varrho(t) = [\varrho_{bH}(t)\ \varrho_{kH}(t)]^T$ reflects the uncertainty associated with measurement and model of Z_H. Furthermore,

$$\alpha_H = \begin{bmatrix}\alpha_{bH} & 0\\ 0 & \alpha_{kH}\end{bmatrix},\quad \beta_H = \begin{bmatrix}\beta_{bH} & 0\\ 0 & \beta_{kH}\end{bmatrix}$$
$$\alpha_A = \begin{bmatrix}\alpha_{bA} & 0\\ 0 & \alpha_{kA}\end{bmatrix},\quad \beta_A = \begin{bmatrix}\beta_{bA} & 0\\ 0 & \beta_{kA}\end{bmatrix} \tag{4}$$

where $\{\alpha_{bH}, \alpha_{kH}, \alpha_{bA}, \alpha_{kA}, \beta_{bH}, \beta_{kH}, \beta_{bA}, \beta_{kA}\}$ are constant parameters. In this paper, we only assumed the uncertainty in estimation of human's bio-mechanics Z_H and did not consider the uncertainty in estimation of human's intent θ_H.

Ideally, to determine an optimal behavior for the automation system, optimization should be performed over all control signals of the automation system, including (i.e., θ_A, Γ_A). However, this paper's focus is to determine Γ_A as a means for allocating the level of authority between the driver and the automation system. By combining Eqs. (1a)–(3b), the dynamics interaction between human and automation system in the lower-level of the adaptive haptic shared control framework can be expressed as following stochastic model:

$$\dot{x}(t) = x(t) + f(x(t), w(t)) + Bu(t) + G\varrho(t) \tag{5a}$$

$$y(t) = h(x(t)) + \varsigma(t) \tag{5b}$$

where $x = [\theta_{SW}\ \dot{\theta}_{SW}\ \theta_S\ \dot{\theta}_S\ B_H\ K_H\ B_A\ K_A]^T$, are the state of the system; $u = [\Gamma_{bA}(t)\ \Gamma_{kA}(t)]^T$ are the control commands, and $w = [\Gamma_{bH}(t)\ \Gamma_{kH}(t)\ \theta_H\ \theta_A\ \tau_V]^T$ are the exogenous signals, $y = [\theta_S\ \dot{\theta}_S\ \tau_T\ K_H\ B_H\ K_A\ B_A]^T$ are measured variables, ς denotes the measurement's noise, and G models the effects of ϱ on the system state, and

$$f(x,w) = \begin{bmatrix}\dot{\theta}_{SW}\\ \frac{B_H(\dot{\theta}_H - \dot{\theta}_{SW}) + K_H(\theta_H - \theta_{SW}) - K_T(\theta_{SW} - \theta_S)}{J_{SW} + J_H}\\ \dot{\theta}_S\\ \frac{\frac{r_S}{r_M}B_A\left(\dot{\theta}_A - \frac{r_S}{r_M}\dot{\theta}_S\right) + \frac{r_S}{r_M}K_A\left(\theta_A - \frac{r_S}{r_M}\theta_S\right) + K_T(\theta_{SW} - \theta_S) + \tau_v}{J_S + \left(\frac{r_S}{r_M}\right)^2 J_M}\\ \alpha_{bH}B_H + \beta_{bH}\Gamma_{bH}\\ \alpha_{kH}K_H + \beta_{kH}\Gamma_{kH}\\ \alpha_{bA}B_A\\ \alpha_{kA}K_A\end{bmatrix}, \tag{6a}$$

$$B = \begin{bmatrix}0 & 0 & 0 & 0 & 0 & 0 & \beta_{bA} & 0\\ 0 & 0 & 0 & 0 & 0 & 0 & 0 & \beta_{kA}\end{bmatrix}^T \tag{6b}$$

$$G = \begin{bmatrix}0 & 0 & 0 & 0 & 1 & 0 & 0 & 0\\ 0 & 0 & 0 & 0 & 0 & 1 & 0 & 0\end{bmatrix}^T \tag{6c}$$

It should be noted that in this paper, we assume all the measured variables y are accessible. In practice, θ_S can be measured using the encoder attached to the steering column, τ_T can be measured using the differential torques indicating the difference between θ_{SW} and θ_S, K_H and B_H can be estimated using various techniques such as identification techniques discussed in [40,41] and K_A and B_A are design parameters and directly can be calculated.

3. Impedance modulation controller design

In this section, we present a predictive controller for modulating the automation's impedance controller parameters. For the steering control problem, we define a nonlinear cost function in the form of

$$\min_{\Gamma_A} J(t) = \mathbb{E}\Big\{ \varphi(x,w) + \int_t^{t+t_h} \mathcal{L}(x,w,u)\, d\varsigma = \int_t^{t+t_h} \{ \|\theta_H - \theta_S\|_{w_1} + \|\theta_A - \theta_S\|_{w_2} + \|\tau_T\|_{w_3} \} d\varsigma \Big\} \tag{7}$$

where t_h is the defined horizon for the model predictive controller, w_1, w_2 and w_3 are weights matrices, $\varphi(x,w)$ is the terminal cost value which is considered zero. The first term of the cost function over the finite horizon (integration part) aims to minimize the error between the human's intent and the steering angle. Similarly, the second term of the cost function over the finite horizon is defined to minimize the tracking error between the automation's desired angle (automation's intent) and the steering angle. Since the human's and automation's intent may not necessarily be the same, which is when the negotiation of control authority becomes important, the third term of the cost function over the finite horizon is defined to minimize the disagreement between a driver and the automation system.

In this paper, we assume that both ϱ and ς to be sequences of independent and identically distributed (i.i.d.) variables with known probability distributions p_ϱ and p_ς, respectively. In particular, $\mathbb{E}[\varrho\varrho^{\mathrm{T}}] = Q_\varrho$, $\mathbb{E}[\varsigma\varsigma^{\mathrm{T}}] = Q_\varsigma$, and $\mathbb{E}[\varrho\varsigma^{\mathrm{T}}] = 0$. Let define, the bar symbol $|\bar{\cdot}|$ on a variable as the expected value (e.g., $\bar{\theta}_S = \mathbb{E}\{\theta_S\}$). Then, the cost function (7) can be expressed as

$$\min_{\Gamma_A} J(t) = \varphi(x,w) + \int_t^{t+t_h} \mathcal{L}(x,w,u)\, d\varsigma = \int_t^{t+t_h} \{ \|\theta_H - \bar{\theta}_S\|_{\hat{w}_1} + \|\theta_A - \bar{\theta}_S\|_{\hat{w}_2} + \|\bar{\tau}_T\|_{\hat{w}_3} \} d\varsigma \tag{8}$$

where $\hat{w}_1 = Q_\varsigma w_1$, $\hat{w}_2 = Q_\varsigma w_2$, and $\hat{w}_3 = Q_\varsigma w_3$.

We define two sets of constraints for the nonlinear cost function J to ensure the non-negative values for the impedance controller's parameters. In particular the expectation form of the inequality constraints are:

$$C_1(t) : \Big\{ s_1^2 - \bar{B}_A(t) = 0,\ \mathbb{E}\{-B_A(t)\} \leqslant 0 \Big\} \tag{9a}$$

$$C_2(t) : \Big\{ s_2^2 - \bar{K}_A(t) = 0,\ \mathbb{E}\{-K_A(t)\} \leqslant 0 \Big\} \tag{9b}$$

Alternatively, constraints in (9a) and (9b) can be defined as chance constraints. Specifically,

$$C_1(t) : \Big\{ \mathbb{P}\Big[-B_A^{(k)} \leqslant 0\Big] \geqslant \mathfrak{V}_{C_1} \Big\} \tag{10a}$$

$$C_2(t) : \Big\{ \mathbb{P}\Big[-K_A^{(k)} \leqslant 0\Big] \geqslant \mathfrak{V}_{C_2} \Big\} \tag{10b}$$

where $\mathfrak{V}_{C_1} \in (0,\ 1)$ and $\mathfrak{V}_{C_2} \in (0,\ 1)$ denote the lower bound of the desired joint probability that the state constraints should satisfy.

To solve the nonlinear cost function described in Eq. (7), we discretize the equation of the dynamics system using the forward Euler method. Specifically,

$$x^{(k+1)} = x^{(k)} + T_s f\left(x^{(k)}, w^{(k)}\right) + T_s B u^{(k)} + T_s G \varrho^k \tag{11}$$

where T_s is the size of the time-step, k is the number of time-step (considered as the current time-step), $x^{(k)}$, $w^{(k)}$ and $u^{(k)}$ are equal to $x(t = T_s k)$, $w(t = T_s k)$ and $u(t = T_s k)$, respectively. It should be noted that higher order discretizations can be employed at the expense of the computational complexity.

Assuming that the system states can be measured at all times, the finite-horizon stochastic MPC (SMPC) problem with probabilistic constraints C_1 and C_2 and cost function J can be stated in discretized mode as follows:

$$\min_{\Gamma_A} J^{(k)} = \sum_{j=1}^{N_p} T_s \{ \|\theta_H^{(k+j)} - \bar{\theta}_S^{(k+j)}\|_{\hat{w}_1} + \|\theta_A^{(k+j)} - \bar{\theta}_S^{(k+j)}\|_{\hat{w}_2} + \|\bar{\tau}_T^{(k+j)}\|_{\hat{w}_3} \}$$

$$\text{s.t. :} \begin{cases} x^{(k+1)} = x^{(k)} + T_s\left(f\left(x^{(k)}, w^{(k)}\right) + B u^{(k)} + G\varrho^k\right) \\ C_1^{(k)} : \{\mathbb{P}\left[-B_A^{(k)} \leqslant 0\right] \geqslant \mathfrak{V}_{C_1}\} \\ C_2^{(k)} : \{\mathbb{P}\left[-K_A^{(k)} \leqslant 0\right] \geqslant \mathfrak{V}_{C_2}\} \end{cases} \tag{12}$$

The closed-loop MPC problem (12) is not solvable directly due to the infinite dimensional nature of the control policy Γ_A. A tractable approximation to (12) can be derived using polynomial chaos (PC) expansion method [32,42]. Using PC expansion, the stochastic function $\psi(\varrho) = f(x,w) + G\varrho$ can be approximated with a finite second-order moments. [31,43]. In particular,

$$\psi(\varrho) = f(x,w) + G\varrho \approx \sum_{j=0}^{L_{pc}-1} \varpi_j \Phi_{\varpi_j}(\varrho) = \eta^{\mathrm{T}} \Lambda(\varrho) \tag{13a}$$

$$\Lambda(\varrho) = \left[\Phi_{\varpi_0},\ \Phi_{\varpi_1},\ \ldots,\ \Phi_{\varpi_{L_{pc}-1}}\right]^{\mathrm{T}} \tag{13b}$$

$$\eta_j = \left[\varpi_0,\ \varpi_1,\ \ldots,\ \varpi_{L_{pc}-1}\right]^{\mathrm{T}} \tag{13c}$$

where ϖ_j indicates the expansion coefficients and $\Phi_{\varpi_j}(\varrho) = \prod_{i=1}^{n} \Phi_{\varpi_{i,j}}(\varrho_i)$ denotes the multivariate polynomials with $\Phi_{\varpi_{i,j}}$ being univariate polynomials in ϱ_i of degree $\varpi_{i,j}$. The total number L_{pc} depends on the number of uncertain parameters and the order of expansion ($L_{pc} = \frac{(n+m)!}{n!m!}$). In this paper, the measurement noises ϱ on the human bio-mechanic parameters B_H and K_H are assumed to have Gaussian distribution in the form of $(\frac{1}{2\pi}\exp\left(-\sigma_i^2/2\right), i \in \{H,\ B\})$. Therefore, the Hermite polynomials can be utilized to approximate nonlinear dynamics (5b). Specifically, the multivariate polynomials with the Gaussian distribution of ϱ becomes $\Lambda(\sigma_i) = [1,\ \sigma_i,\ \sigma_i^2 - 1,\ \sigma_i^3 - 3\sigma_i,\ \sigma_i^4 - 6\sigma_i^2 + 3, \ldots]$ and the expansion coefficients ϖ_j at each time state can be calculated based on the pseudo-spectral approach [44]. The details of PC expansion method can be found in [45]. By employing PC expansion, the deterministic surrogate for the stochastic MPC problem (12) can be expressed as follow:

$$\min_{\Gamma_A} J^{(k)} = \sum_{j=1}^{N_p} T_s \{ \|\theta_H^{(k+j)} - \bar{\theta}_S^{(k+j)}\|_{\hat{w}_1} + \|\theta_A^{(k+j)} - \bar{\theta}_S^{(k+j)}\|_{\hat{w}_2} + \|\bar{\tau}_T^{(k+j)}\|_{\hat{w}_3} \}$$

$$\text{s.t. :} \begin{cases} \bar{x}^{(k+1)} = \bar{x}^{(k)} + T_s\left(\left(\eta^{(k)}\right)^T \Lambda\left(\varrho^{(k)}\right) + B u^{(k)}\right) \\ C_1^{(k)} : -\sqrt{\frac{\mathfrak{V}_{C_1}}{1-\mathfrak{V}_{C_1}}}\ \mathrm{Var}[B_A^{(k)}] - \bar{B}_A^{(k)} + s_1 = 0 \\ C_2^{(k)} : -\sqrt{\frac{\mathfrak{V}_{C_2}}{1-\mathfrak{V}_{C_2}}}\ \mathrm{Var}[K_A^{(k)}] - \bar{K}_A^{(k)} + s_2 = 0 \end{cases} \tag{14}$$

where s_1 and s_2 are slack variables and Var[.] represent the variable's variance. By using the non-negative slack variables in Eq. (14), the inequality constraints will be transformed to the equality constraints [46].

Next, Let H denote the Hamiltonian defined by

$$H\left(\bar{x}^{(k)}, w^{(k)}, u^{(k)}, \lambda^{(k)}, \mu^{(k)}\right) = T_s\left(\|\theta_H^{(k)} - \bar{\theta}_S^{(k)}\|_{\hat{w}_1} + \|\theta_A^{(k)} - \bar{\theta}_S^{(k)}\|_{\hat{w}_2} + \|\bar{\tau}_T^{(k)}\|_{\hat{w}_3}\right) + \lambda^{(k)}\left(\bar{x}^{(k)} - \bar{x}^{(k+1)} + T_s\left(\left(\eta^{(k)}\right)^T \Lambda\left(\varrho^{(k)}\right) + B u^{(k)}\right)\right) + \mu^{(k)}\left(\left[C_1^{(k)}, C_2^{(k)}\right]^{\mathrm{T}}\right) \tag{15a}$$

where

$$\lambda^{(k)} = \left[\lambda_{\theta_S}^{(k)}\ \ \lambda_{\dot{\theta}_S}^{(k)}\ \ \lambda_{\theta_{SW}}^{(k)}\ \ \lambda_{\dot{\theta}_{SW}}^{(k)}\ \ \lambda_{\Gamma_{bH}}^{(k)}\ \ \lambda_{\Gamma_{kH}}^{(k)}\ \ \lambda_{\Gamma_{bA}}^{(k)}\ \ \lambda_{\Gamma_{kA}}^{(k)}\right] \tag{15b}$$

$$\mu^{(k)} = \begin{bmatrix} \mu_{C_1}^{(k)} & \mu_{C_2}^{(k)} \end{bmatrix} \tag{15c}$$

where λ and μ are costate vector and Lagrange multiplier vector respectively. The necessary conditions for optimality are obtained by the calculus of variations [47]. We discretize the conditions by dividing the horizon into N_p steps. The discretized Karush–Kuhn–Tucker (KKT) necessary conditions are given as follows:

$$\bar{x}^{*(k+1)} = \bar{x}^{*(k)} + T_s \left(\left(\eta^{*(k)}\right)^T \Lambda\left(\varrho^{(k)}\right) + B u^{*(k)} \right) \tag{16a}$$

$$\bar{x}^{*(0)} = \bar{x}^{(0)} \tag{16b}$$

$$\lambda^{*(k)} = \lambda^{*(k+1)} + T_s \frac{\partial H^T\left(\bar{x}^{*(k)}, w^{(k)}, u^{*(k)}, \lambda^{*(k)}, \mu^{*(k)}\right)}{\partial \bar{x}} \tag{16c}$$

$$\lambda^{*(k+N_p)} = 0 \tag{16d}$$

$$\frac{\partial H^T\left(\bar{x}^{*(k)}, w^{(k)}, u^{*(k)}, \lambda^{*(k)}, \mu^{*(k)}\right)}{\partial u} = 0 \tag{16e}$$

$$\begin{bmatrix} C_1^{(k)} \\ C_2^{(k)} \end{bmatrix} = \begin{bmatrix} 0 \\ 0 \end{bmatrix} \tag{16f}$$

By employing forward recursion, for $j = 1, \ldots, N_p$, the state variables $\bar{x}^{*(k+j)}$, can be defined using Eqs. (16a) and (16b). Furthermore, by employing back recursion from the final condition to the present time-step ($j = N_p, N_p - 1, \ldots, 1$) the co-states $\lambda^{*(k+j)}$ can be determined using (16c) and (16d). Finally, by plugging $\bar{x}^{*(k+j)}$ and $\lambda^{*(k+j)}$ into Eqs. (16e) and (16f), a KKT vector $F(X,U,t)$ for N_p horizon can be defined, where

$$F = \begin{bmatrix} \frac{\partial H^T\left(\bar{x}^{*(k)}, w^{(k)}, u^{*(k)}, \lambda^{*(k)}, \mu^{*(k)}\right)}{\partial u} \\ C_1^{(k)} \\ C_2^{(k)} \\ \vdots \\ \frac{\partial H^T\left(\bar{x}^{*(k+N_c)}, w^{(k+N_c)}, u^{*(k+N_c)}, \lambda^{*(k+N_c)}, \mu^{*(k+N_c)}\right)}{\partial u} \\ C_1^{(k+N_c)} \\ C_2^{(k+N_c)} \\ \vdots \\ \frac{\partial H^T\left(\bar{x}^{*(k+N_p)}, w^{(k+N_p)}, u^{*(k+N_p)}, \lambda^{*(k+N_p)}, \mu^{*(k+N_p)}\right)}{\partial u} \\ C_1^{(k+N_p)} \\ C_2^{(k+N_p)} \end{bmatrix} \tag{17a}$$

where

$$X = [\bar{x}^{(k)}, w^{(k)}, \bar{x}^{(k+1)}, w^{(k+1)}, \ldots, \bar{x}^{(k+N_p)}, w^{(k+N_p)}]^T \tag{17b}$$

$$U = [u^{(k)}, \mu^{(k)}, \ldots, u^{(k+N_c)}, \mu^{(k+N_c)}, \ldots, u^{(k+N_c)}, \mu^{(k+N_p)}]^T \tag{17c}$$

where N_c is the number of the control horizon steps. Note that for $N_c \le j \le N_p$, $u^{k+j} = u^{k+N_c}$. By solving a nonlinear algebraic equation $F(X,U,t) = 0$, an optimal points can be determined and the optimal control command can be determined by

$$u^{(k)} = P_0 U \tag{18}$$

where P_0 is a projection matrix and can be defined as

$$P_0 = \begin{bmatrix} 1 & 0 & 0 & \cdots & 0 & 0 & 0 \\ 0 & 1 & 0 & \cdots & 0 & 0 & 0 \end{bmatrix}_{2\times 12N_p}. \tag{19}$$

3.1. Continuation method

To solve $F(X,U,t) = 0$ with respect to the unknown vector U, for each time-step, the C/GMRES method is employed [38]. In C/GMRES method, instead of solving $F(X,U,t) = 0$, we select the proper initial value $U(0)$ and take the time derivative of Eq. (17a) into account. Specifically, we define

$$\dot{F}(X,U,t) = A_s F(X,U,t) \tag{20}$$

where A_s is a stable matrix (i.e. with negative eigenvalues). Differentiating the left side of Eq. (20) yields

$$F_U(X,U,T)\dot{U} = A_s F(X,\ U,\ t) - F_X(X,U,t)\dot{X} - \dot{F}(X,U,t) \tag{21}$$

If F_U is non singular, we can obtain the differential equation for $\dot{U}$ as

$$\dot{U} = F_U^{-1}\left(A_s F(X,\ U,\ t) - F_X(X,U,T)\dot{X} - \dot{F}(X,U,T)\right) \tag{22}$$

3.2. Forward difference GMRES method

The calculation of Jacobians F_x, F_U and $\dot{F}$ is computationally expensive. Instead to solve Eq. (22), we employed the forward-difference approximation to eliminate the calculation of the Jacobians. To this end, using the concept of forward difference, we approximate the products of Jacobians and some $L \in \mathbb{R}^{11\times N_p}$, $M \in \mathbb{R}^{12\times N_p}$, and $\omega \in \mathbb{R}$ and replaced it to Eq. (22) which results in:

$$D_h F\left(X,U,t:0,\dot{U},0\right) = b\left(X,\dot{X},U,t\right) \tag{23a}$$

where

$$b\left(X,\dot{X},U,t\right) = A_s F(X,U,t) - D_h F\left(X,U,t:\dot{X},0,1\right) \tag{23b}$$

$$D_h F(X,U,t:L,M,\omega) = \frac{F(X+hL,U+hM,t+h\omega) - F(X,U,t)}{h} \tag{23c}$$

where h is a positive real number, $D_h F(X,U,t:L,M,\omega)$ stands for the concept of forward difference for F. It should be noted that there is main difference between forward-difference approximation and finite-difference approximation with regards to computational expenses. The forward difference approximation of the products of the Jacobians and vectors can be calculated with only an additional evaluation of the function, which requires notably less computational burden than approximation of the Jacobians themselves. Since Eq. (23a) is a linear equation with respect to $\dot{U}$, we applied the forward difference GMRES method to solve it [37]. The details of this method is described in Algorithm 1.

Algorithm 1: Forward-Difference GMRES[38]

Result: $\dot{U} := \mathrm{FDGMRES}\left(X,\dot{X},U,U_{\mathrm{int}},h,\mathcal{I}_{\max}\right)$
$\hat{r} := b\left(X,\dot{X},U,t\right) - D_h F\left(X + h\dot{X},U,t+h:0,U_{\mathrm{int}},0\right)$;
$v_1 := \hat{r}/\|\hat{r}\|$, $\rho := \|\hat{r}\|$, $\zeta := \rho$, $\mathcal{I} = 0$;
while $\mathcal{I} < \mathcal{I}_{\max}$ **do**
  $\mathcal{I} := \mathcal{I} + 1$;
  $v_{\mathcal{I}+1} := D_h F\left(X + h\dot{X},U,t+h:0,v_{\mathcal{I}},0\right)$;
  for $j = 1,2,\ldots,\mathcal{I}$ **do**
    $h_{j,\mathcal{I}} := v_{\mathcal{I}+1}^T v_j$;
    $v_{\mathcal{I}+1} := v_{\mathcal{I}+1} - h_{j,\mathcal{I}} v_j$
  end
  $h_{\mathcal{I}+1,\mathcal{I}} := \|v_{\mathcal{I}+1}\|$;
  $v_{\mathcal{I}+1} := v_{\mathcal{I}+1}/\|v_{\mathcal{I}+1}\|$;
  for $e_1 = [1,0,\ldots,0] \in \mathbb{R}^{\mathcal{I}+1}$ && $H_{\mathcal{I}} = (h_{i,j}) \in \mathbb{R}^{\mathcal{I}+1\times\mathcal{I}}$ **do**
    Minimize $\|\zeta e_1 - H_{\mathcal{I}}\mathcal{Y}^{\mathcal{I}}\|$ with LS method to determine $\mathcal{Y} \in \mathbb{R}^{\mathcal{I}}$
  end
  $\rho := \|\zeta e_1 - H_{\mathcal{I}}\mathcal{Y}^{\mathcal{I}}\|$;
end
$\dot{U} := \dot{U} + V_{\mathcal{I}}\mathcal{Y}^{\mathcal{I}}$ where $V_{\mathcal{I}} = [v_1, v_2, \cdots, v_{\mathcal{I}}] \in \mathbb{R}^{12\times N_p\times\mathcal{I}}$.

3.3. Combination of continuation and GMRES

$\dot{U}$ is the output of the forward-difference GMRES algorithm, and integration of this value results in U for the current time step. For

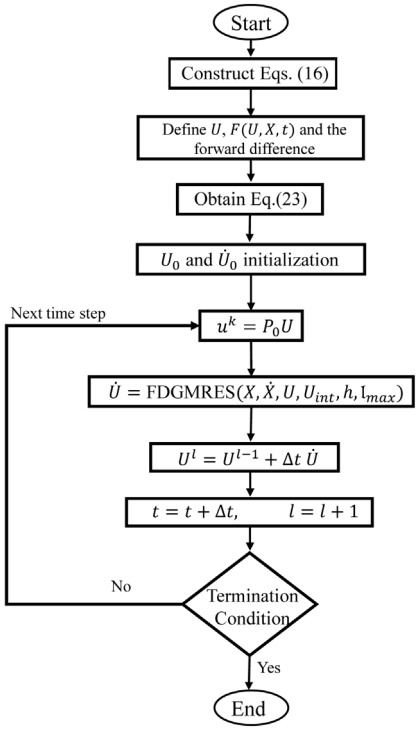

Fig. 3. C/GMRES method's flowchart.

a sampling time $\triangle t$ and integer value ℓ, Algorithm 2 shows the required steps of the continuation/GMRES method for nonlinear model predictive control.

Algorithm 2: Continuation/GMRES [38]

Result: $U := \text{CntFDGMRES}\big(X, \dot{X}, \dot{U}, t, \triangle t, \delta\big)$
(1) $t := 0,\ \ell := 0$;
(2) Select small value $\delta > 0$;
(3) Find $U(0)$ for satisfying $\|F(X(0), U(0), 0)\| \leqslant \delta$;
(4) In $t' \in [t, t + \triangle t)$ set $u(t') := P_0 U(\ell \triangle t)$;
At time $t + \triangle t$ by considering measured states $x(t + \triangle t)$ set
$\triangle x_\ell = x_\ell(t + \triangle t) - x_\ell(t)$;
(5) $U_{\text{int}} = U_{t_0}$, $U_{\text{int}} = \dot{U}((\ell - 1) \triangle t)$;
(6) $\dot{U}(\ell \triangle t) := \text{FDGMRES}\big(X, \triangle x_\ell / \triangle t, U, U_{\text{int}}, h, I_{\max}\big)$;
(7) Set $U\big((\ell + 1) \triangle t\big) = U\big(\ell \triangle t\big) + \triangle t\ \dot{U}\big(\ell \triangle t\big)$
(8) Set $t := t + \triangle t,\ \ell := \ell + 1$ and go back to line (4)

It should be noted that the C/GMRES is an iterative method that solves Eq. (17a) with respect to $\dot{U}$ only once at each sampling time and therefore, requires much less computational expenses than other iterative methods such as Newton's method. Moreover, C/GMRES involves no line search, which is also a significant difference from standard optimization methods [38]. The C/GMRES method's flowchart is depicted in Fig. 3, which demonstrates the solving procedure for each time steps in the numerical executions. The problem construction step till $U, \dot{U}_0$ initialization will be executed one time in the algorithm, which leads to a reduced computational load in the solver. The rest of the algorithm is running till the termination condition is satisfied. The termination condition in the numerical simulation is the simulation run time, and in the PIL implementations, it is set as the maximum number of control loop execution.

Fig. 4 shows the control architecture of the closed loop. The higher-level control consists of four main sections: interaction mode determination that define the appropriate form of the cost function as well as the appropriate weights of each term in the cost function [21,48,49], human's biomechanics identification that identifies the current state of Z_{H} [40,41,50], human's intent detection that determines θ_{H}

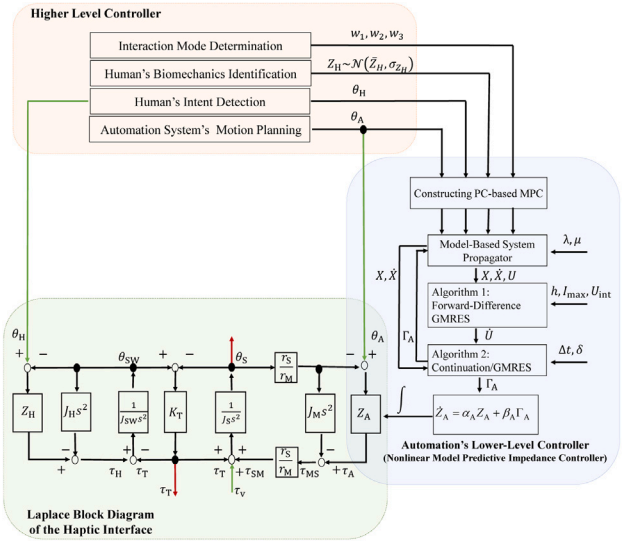

Fig. 4. The detailed block diagram of the adaptive haptic shared control paradigm including the higher level controller, the automation's lower-level controller and Laplace block diagram of the haptic interface.

[12–14] and automation system's motion planning that determine θ_{A} [51]. The outputs of the higher-level controller are fed to the automation's lower-level control to determine the optimal Z_{A}. By modulating the automation's impedance controller gains, the control authority dynamically exchanges between the human and automation, and subsequently θ_{S} follows the intents of humans or automation.

4. Simulation studies and discussions

In this section, we present a series of simulation studies demonstrating the effectiveness of the proposed controller in transferring the control authority between the driver and the automation system. The following simulations consider a scenario where the human and the automation system detect an obstacle and negotiate on controlling the steering wheel so that the obstacle can be avoided safely. To this end, the simulations involve two conditions when the control authority shifts from the human to the automation system (active safety mode), as well as when the control authority shifts from the automation system to human (assistive mode). Also, we included two other conditions where the human and automation are in cooperative and uncooperative mode. In cooperative mode, the human and automation intents detect the obstacle and decide to avoid the obstacle by maneuvering in the same direction (same intent signs $\text{sgn}(\theta_{\text{H}}) = \text{sgn}(\theta_{\text{A}})$). In uncooperative mode, humans and automation's detect the obstacle but their intents have opposite signs ($\text{sgn}(\theta_{\text{H}}) = -\text{sgn}(\theta_{\text{A}})$). In this paper, the driver's intent is expressed by the following curve

$$\theta_{\text{H}} = \begin{cases} 0 & t < T_1 \\ \frac{W}{2}\cos\left(\frac{\pi}{T_2}t - \frac{T_{1,2}}{T_2}\pi\right) + \frac{W}{2} & T_1 < t < T_{1,2} \\ W & T_{1,2} < t < T_{1,2,3} \\ \frac{W}{2}\cos\left(\frac{\pi}{T_2}t - \frac{T_{1,2,3}}{T_2}\pi\right) + \frac{W}{2} & T_{1,2,3} < t < T_{1,2,3} + T_2 \\ 0 & T_{1,2,3} + T_2 < t. \end{cases} \tag{24}$$

$$T_{1,2} = T_1 + T_2, \qquad T_{1,2,3} = T_1 + T_2 + T_3$$

where $T_1 = 1$ sec, $T_2 = 5$ sec, $T_3 = 2$ sec and $W = 1$ rad are selected for the following examples. Note that in the following examples to illustrate the results clearly, we select $|\theta_{\text{A}}| = 0.9|\theta_{\text{H}}|$. We also assume no feedback from the road and consider $\tau_{\text{V}} = 0$ in the following examples.

Additionally, in the following simulations, we select the mean values of human arms' bio-mechanics as either $\bar{Z}_{\text{H}} = [0.5\ 1]^{\text{T}}$ representing

a case when the human control command is sufficient or $\bar{Z}_H = [0.1\ 0.1]^T$ describing a situation when the driver's control command is insufficient. These values are selected based on a set of simulation studies. To consider the role of uncertainity in the estimation of the human's bio-mechanics parameters, K_H and B_H are generated using a series of random parameter vectors generated from the Gaussian pdfs [52]. Specifically, the human's bio-mechanics variance value $\left(\sigma_{B_H},\ \sigma_{K_H}\right)$ in random parameter vectors has maximum $(0.05,\ 0.1)$ to define the performance range of the adaptive impedance controller. The additive disturbances ϱ have a Gaussian distribution $\varrho \sim \mathcal{N}\left(0,\ Q_\sigma\right)$ with zero mean and covariance matrix $Q_\sigma = diag[0.01,\ 0.001,\ 0.005,\ 0.05,\ 0.02, 0,\ 0]$. The numerical values for the other parameters in the simulation studies are demonstrated in Table 1.

When the human's control command is sufficient (high Z_H), the automation system shall be designed to yield the control authority to the human operator. Specifically, we select the weights of the cost function to be $w_1 = 0.2, w_2 = 0$ and $w_3 = 0.8$. With selecting these weights for the cost function, the automation system acts in an assistive mode [2]. On the other hand, when the human's control command is insufficient (low Z_H), the automation system is designed to ensure the safety of the task by avoiding the obstacle. In particular, we select the weights of the cost function to be $w_1 = 0, w_2 = 0.8$ and $w_3 = 0.2$. With choosing these weights for the cost function, the automation system acts in the active safety mode [2].

Fig. 5 demonstrates the problem of control authority negotiation in uncooperative mode. Specifically, the interaction between the human and automation system in the adaptive haptic shared control paradigm is compared with the interaction in non-adaptive haptic shared control wherein the parameters of the automation's impedance controller are invariant. The first row shows the human's intent θ_H, the automation's intent θ_A, and the steering angle θ_S. The second row shows the human's torque τ_H, the automation system's torque τ_A, and the torque measured by the torque sensor τ_T. The third and fourth row shows the parameters of the damping and stiffness of the human arm and automation's impedance controller, respectively. In this example, we select the human's biomechanics mean value to be $\bar{Z}_H = [0.5\ 1]^T$. Since with $\bar{Z}_H = [0.5\ 1]^T$, the human's control command is sufficient to maneuver the steering angle safely, we select the weights of the cost function such that the automation acts in an assistive mode [2] (i.e., $w_1 = 0.2, w_2 = 0$ and $w_3 = 0.8$). In a non-adaptive haptic shared control paradigm, the automation's impedance controller parameters are selected to be the same as the mean value of the driver's biomechanics ($\bar{Z}_H = Z_A$). It follows from Fig. 5-A and 5-B that in the non-adaptive haptic shared control paradigm when humans and automation are in the uncooperative mode, their control commands are opposite and cancel out each other ($\tau_A \approx -\tau_H$); and therefore, the steering angle is almost zero ($\bar{\theta}_S \approx 0$). On the other hand, it follows from Figs. 5-C and 5-D that in the adaptive haptic shared control paradigm, the automation' impedance controller parameters Z_A are reduced to minimize the disagreement τ_T. It follows from Fig. 5-B that the disagreement between humans and automation is effectively smaller than the non-adaptive haptic shared control paradigm. Furthermore, since the human's adopted impedance is sufficient, the steering angle θ_S command follows the human's intent θ_H.

Fig. 6 also demonstrates the interaction between the driver and the automation system in the uncooperative mode in non-adaptive and adaptive haptic shared control paradigms. In this example, we selected the human's biomechanics to be $\bar{Z}_H = [0.1\ 0.1]^T$. Since with $\bar{Z}_H = [0.1\ 0.1]^T$, the human's control command is insufficient to maneuver the steering angle safely, we select the weights of the cost function such that the automation acts in an active safety mode [2] (i.e., $w_1 = 0, w_2 = 0.8$ and $w_3 = 0.2$). Similar to the previous example, we assumed the automation system has an estimation of the human's bio-mechanics, and since the human adopted a lower impedance, the automation re-gain the control authority from the human driver. Also, similar to the previous example, in the non-adaptive paradigm, the automation's impedance controller parameters are selected to be the same as the driver, and therefore, the control commands of the human τ_H and automation system τ_A are opposite and cancel out each other (see Fig. 6-A). On the other hand, it follows from the Figs. 6-C and 6-D that in the adaptive haptic shared control paradigm, the automation system's impedance controller parameters Z_A is increased to ensure the desired performance (e.g., avoiding an obstacle in the middle of the road). Since the automation's impedance control parameters are increased, the disagreement τ_T between the two agents is also increased (See Fig. 6-B). Furthermore, since Z_A is bigger than Z_H, the steering angle θ_S is closer to the automation's intent θ_A (see Fig. 6-A).

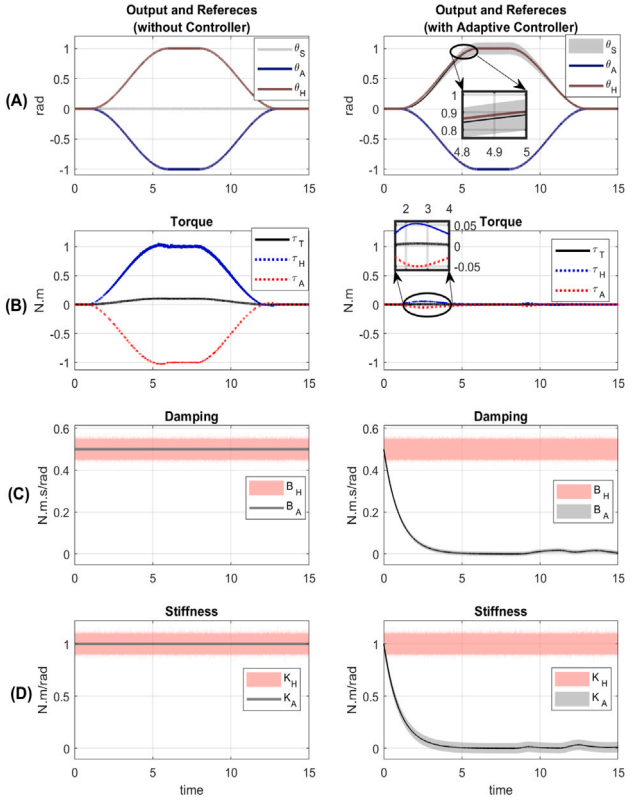

Fig. 5. The outputs of the driver and automation system interaction within non-adaptive and adaptive haptic shared control paradigms are compared. (A) driver intent (red), autonomous system intent (blue) and steering column angle (black) (B) Measured torque (black), human torque (red) and automation torque (blue) (C) Damping coefficients of the agents (D) Stiffness coefficients of the agents. The automation system act as assistive in an uncooperative mode in the adaptive haptic shared control paradigm. By reducing the automation's impedance controller gains, the automation system reduces the disagreement between the human and automation system. The shaded bands for θ_S, K_A, and B_A represent the 95% confidence intervals. (For interpretation of the references to color in this figure legend, the reader is referred to the web version of this article.)

Fig. 7 demonstrates the interaction between the driver and the automation system in the cooperative mode. In this example, we select the human's biomechanics to be $\bar{Z}_H = [0.5\ 1]^T$. Since the human's control command is sufficient to maneuver the steering wheel safely, we select the weights of the cost function as $w_1 = 0.2, w_2 = 0$, and $w_3 = 0.8$. With choosing these weights for the cost function, the automationsystem acts in an assistive mode [2]. In a non-adaptive haptic shared control paradigm, the automation's impedance controller parameters are selected to be the same as the driver ($Z_A = \bar{Z}_H$). Although the torques of the driver τ_H and the automation system τ_A in cooperative mode are much smaller than torques in the uncooperative mode, it follows from the Figs. 7-B that by modulating the automation' impedance controller parameters Z_A the disagreement τ_T even decreased more.

Table 1
Numerical values for the system parameters in the simulation.

Parameters	Variables	Interaction modes		Unit
		Active safety	Assistive	
Activation coefficient of k_A	β_{k_A}	1	0.1	–
Activation coefficient of b_A	β_{b_A}	1	0.1	–
Memory coefficient of k_A	α_{k_A}	−1		–
Memory coefficient of b_A	α_{k_A}	−1		–
Driver arm's stiffness	K_H	0.1	1	–
Driver arm's damping	B_H	0.1	0.5	–
Driver arm's inertia	J_H	1×10^{-3}		Kg m^2
Steering wheel inertia	J_{SW}	1×10^{-2}		Kg m^2
Steering column inertia	J_S	1×10^{-2}		Kg m^2
Motor's inertia	J_M	1×10^{-3}		Kg m^2
Torque sensor stiffness	K_T	1000		N m/rad
Timing belt mechanical advantage	r_S/r_M	1		–
Prediction horizon	N_p	10		–
Control horizon	N_c	10		–
The sample time	T_S	1×10^{-2}		s
Maximum index	$\mathcal{I}_{max}$	12		–
KKT vector norm range	δ	5×10^{-2}		–

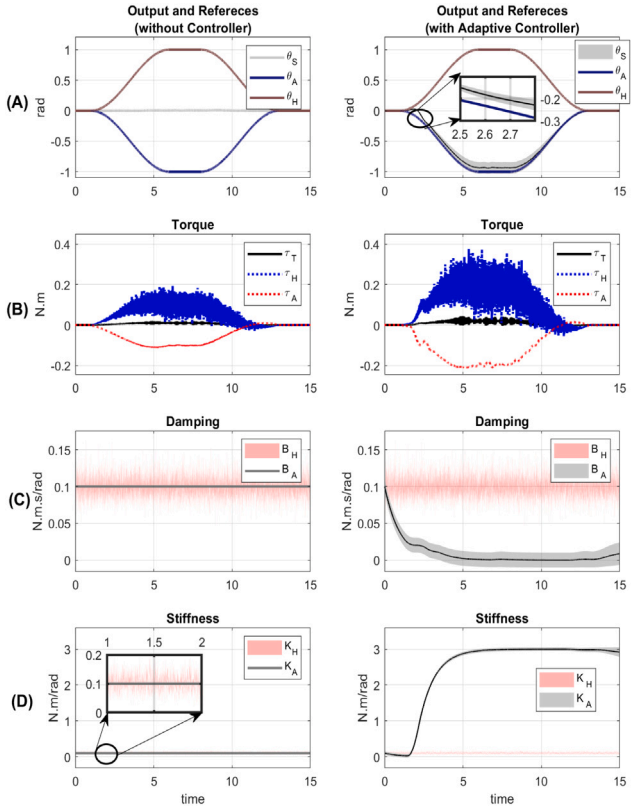

Fig. 6. The outputs of the driver and automation system interaction within non-adaptive and adaptive haptic shared control paradigms are compared. (A) driver intent (red), autonomous system intent (blue) and steering column angle (black) (B) Measured torque (black), human torque (red) and automation torque (blue) (C) Damping coefficients of the agents (D) Stiffness coefficients of the agents. The automation system act as assistive in an uncooperative mode in the adaptive haptic shared control paradigm. The automation system provides enough control input for obstacle avoidance by increasing the automation's impedance controller gains. The shaded bands for θ_S, K_A, and B_A represent the 95% confidence intervals. (For interpretation of the references to color in this figure legend, the reader is referred to the web version of this article.)

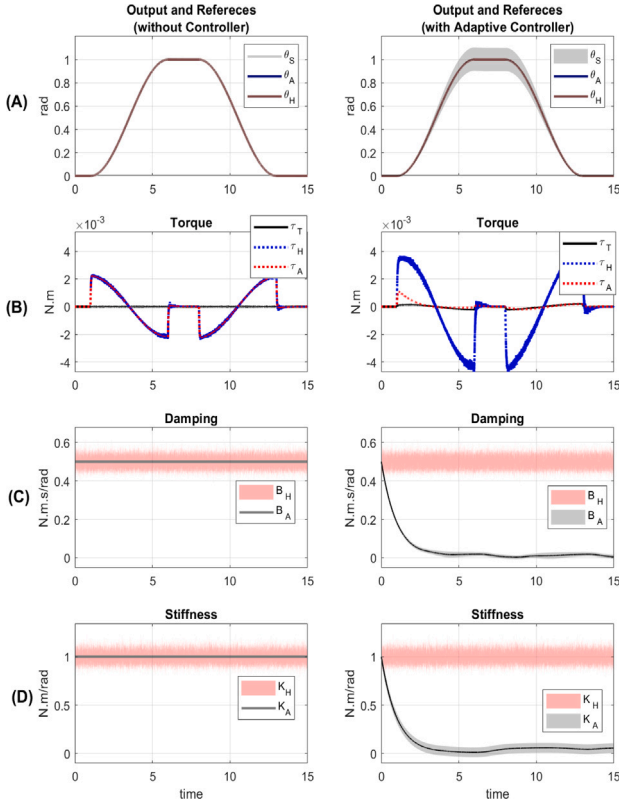

Fig. 7. The outputs of the driver and automation system interaction within non-adaptive and adaptive haptic shared control paradigms are compared. (A) driver intent (red), autonomous system intent (blue) and steering column angle (black) (B) Measured torque (black), human torque (red) and automation torque (blue) (C) Damping coefficients of the agents (D) Stiffness coefficients of the agents. The automation system act as assistive in a cooperative mode in the adaptive haptic shared control paradigm. By reducing the automation's impedance controller gains, the automation system reduces the disagreement between the human and automation system. The shaded bands for θ_S, K_A, and B_A represent the 95% confidence intervals. (For interpretation of the references to color in this figure legend, the reader is referred to the web version of this article.)

Fig. 8 also demonstrates the interaction between the driver and the automation system in non-adaptive and adaptive haptic shared control paradigms in the cooperative mode. In this example, we select the human's biomechanics to be $\bar{Z}_H = [0.1\ 0.1]^T$. Since the human's control command is insufficient to maneuver the steering wheel safely, we select the weights of the cost function to be $w_1 = 0, w_2 = 0.8$, and $w_3 = 0.2$. With choosing these weights for the cost function, the automation system acts in the active safety mode [2]. It follows from the Figs. 8-C and 8-D that in the adaptive haptic shared control paradigm, the automation' impedance controller parameters Z_A are increased to

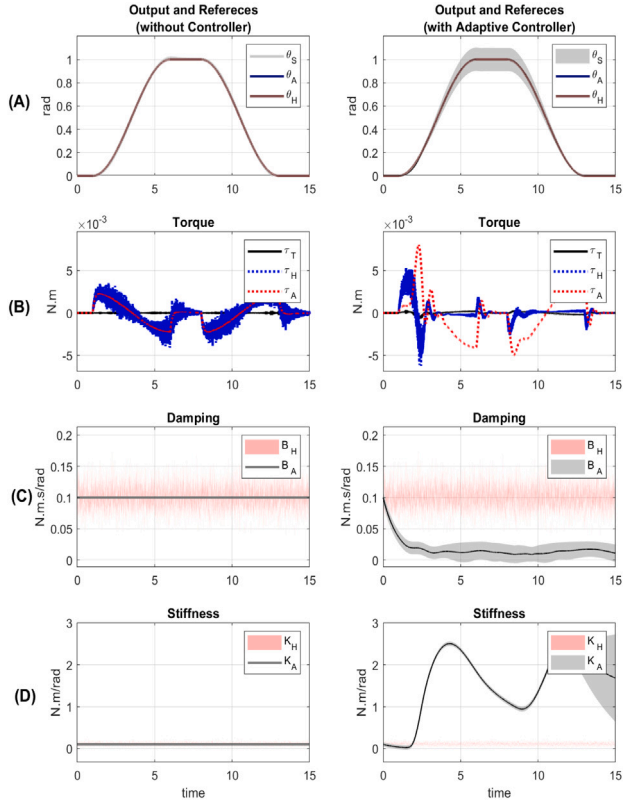

Fig. 8. The outputs of the driver and automation system interaction within non-adaptive and adaptive haptic shared control paradigms are compared. (A) driver intent (red), autonomous system intent (blue) and steering column angle (black) (B) Measured torque (black), human torque (red) and automation torque (blue) (C) Damping coefficients of the agents (D) Stiffness coefficients of the agents. The automation system act as active safety in a cooperative mode in the adaptive haptic shared control paradigm. By increasing the automation's impedance controller gains, the automation system provides enough control input for obstacle avoidance. The shaded bands for θ_S, K_A, and B_A represent the 95% confidence intervals. (For interpretation of the references to color in this figure legend, the reader is referred to the web version of this article.)

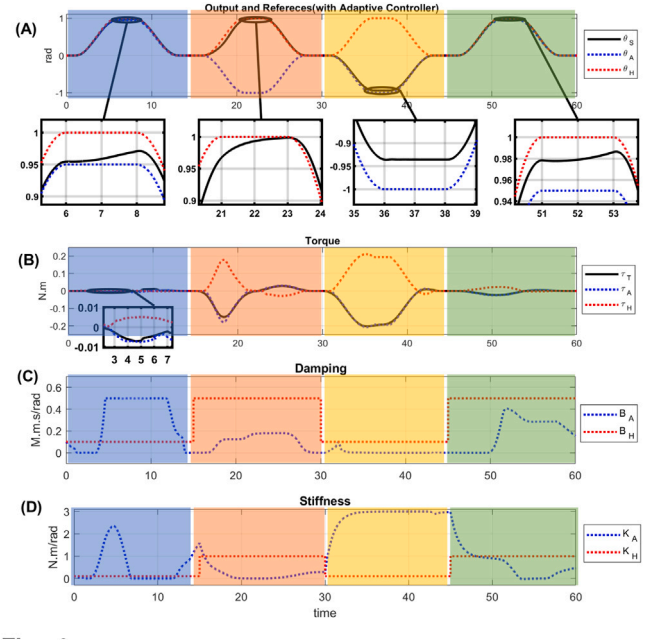

Fig. 9. The human and automation's interaction in the four interaction modes. The sequence of these interaction modes is cooperative–active safety (shaded blue), uncooperative assistive (shaded orange), uncooperative–active safety (shaded yellow), and cooperative-autopilot mode (shaded green). The outputs of the driver and automation system interaction within non-adaptive and adaptive haptic shared control paradigms are compared. (A) driver intent (red), autonomous system intent (blue) and steering column angle (black) (B) Measured torque (black), human torque (red) and automation torque (blue) (C) Damping coefficients of the agents (D) Stiffness coefficients of the agents. In the proposed adaptive haptic shared paradigm, by recognizing the interaction mode, the appropriate set of weights for the cost function can be determined, and automation can continuously adjust its impedance controller parameters such that not only the safety is ensured, but also the customizability feature of the automation system is improved. (For interpretation of the references to color in this figure legend, the reader is referred to the web version of this article.)

ensure the desired performance (e.g., providing the required control inputs).

Considering no uncertainty in Z_H (i.e., $Z_H = \bar{Z}_H$), Fig. 9 shows a scenario wherein all the four interaction modes are integrated into one unified framework. The sequence of these interaction modes is cooperative–active safety, uncooperative assistive, uncooperative–active safety, and cooperative-autopilot mode. It follows from Fig. 9 that initially, the human and automation system are in cooperative mode; however, the human's torque input is insufficient (low Z_H). The automation system increases its impedance to provide the required control command. In the next mode, the human and robot are in the uncooperative mode; however, the human's torque input is sufficient (high Z_H). The automation system reduces its impedance to minimize the disagreement with the driver. In the third mode, the human and robot are in the uncooperative mode; however, the human's torque input is insufficient (low Z_H). The automation system again increases its impedance to ensure safety at the expense of fighting with the driver (high τ_T). Finally, the human and robot are again in the cooperative mode in the fourth mode; however, the human's torque input is sufficient (high Z_H). The automation system reduces its impedance and yields the control authority to the driver. It follows from Fig. 9 that in the proposed adaptive haptic shared paradigm, by recognizing the interaction mode, the appropriate set of weights for the cost function can be determined and automation can continuously adjust its impedance controller parameters such that not only the safety is ensured, but also the customizability feature of the automation system is improved.

5. PIL implementation

To validate the modulation algorithms developed in this paper in a human-in-the-loop setup, it is necessary to make sure the nonlinear model predictive algorithms can be solved in real-time. As a first step towards this goal, we performed a series of tests with a processor in the loop (PIL) using a set of low-cost microcontrollers.

The processor in the loop (PIL) is a test method with a compiled code that describes a controller running in an external microprocessor or processor. The deterministic plant model runs on a remote simulator. Both subsystems, controller and plant, are linked by a communication link or data transfer port. A PIL platform is developed for the proposed impedance modulation approach and illustrated in Fig. 10-(A). In PIL simulations, subsystems run in separate processing platforms, which intercross input and output data through a communication mean.

In PIL architecture, we select the ATMega2560 and STM32F4 discovery board to be the target boards for implementation purposes. The PIL test-bed block diagram is illustrated in Fig. 10. As illustrated in Fig. 10-B), the target board contains three main subroutines. The port decoder subroutine extracts the host computer's received data for the nonlinear MPC. The NLMPC subroutine, based on the current value of the state/co-state vector and the unknown vector on the previous time step, propagates the system to form the $F_{L,A}(X_{LL}, U_{LL}, t)$. Then the optimal value of the unknown vector from the C/GMRES method will be defined and based on (18), the control signal u_{LL} will be fed

Table 2
PIL results for the Low-level controller in active safety and assistive modes.

	Grid Num. (N_p)	Arduino Mega2560			STM32F4 Discovery		
		Maximum C/GMRES Iteration					
		10 (Itr)	15 (Itr)	20 (Itr)	10 (Itr)	15 (Itr)	20 (Itr)
Active Safety Mode	10	280	410	570	80	110	150
	20	420	630	910	120	160	230
	30	620	980	1380	170	250	400
Assistive mode	10	210	390	510	70	90	130
	20	370	590	860	100	140	210
	30	580	910	1210	150	230	370

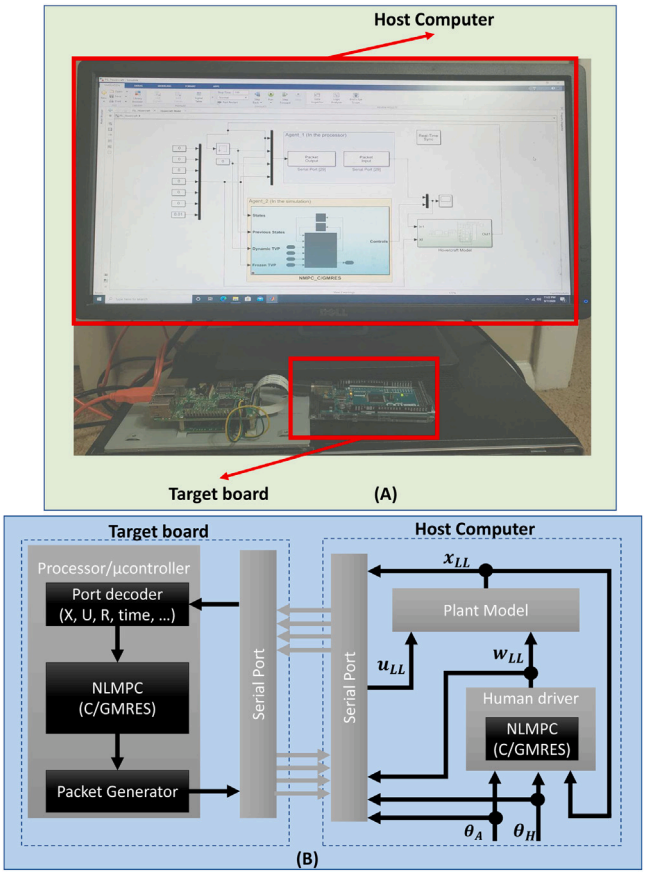

Fig. 10. (A) The experimental PIL test setup, (B) The block diagram of the PIL setup.

to the packet generator subroutine. The communication between the target board and the Simulink environment is performed over a serial port connection by 115200 bps. The host and target modules' synchronization procedure is based on the control loop execution on the target board. Arduino Mega's processor is an ATmega2560 microcontroller, and its CPU clock is 16 MHz, while the STM32F4 has up to 180 MHz operating frequency. Different scenarios are implemented in the PIL test-bed for each of these processors based on the 10, 20, and 30 grid numbers N_p and 10, 15, and 20 maximum iterations C/GMRES solver.

The PIL implementation for low-level controllers is performed for both active safety and assistive modes. The control loop's execution time on a microcontroller depends on the interaction mode (assistive or active-safety modes). For example, On the discover board with grid number 10 and the maximum C/GMRES iteration 15, the execution time for the active-safety and assistive modes are 110 and 90 microseconds, respectively (Table 2). The maximum iterations for the continuation method and the horizon view (grid number) are the main effective parameters in the control loop's execution time. The termination condition for convergence in GMRES method is in the range of 10^{-4} for both control signals (Γ_{kA}, Γ_{bA}). For each microcontroller in each mode, nine case studies are performed. Specifically, we considered three values for the maximum C/GMRES iteration and three values of the grid numbers (N_p). Table 2 shows the PLI results for both microcontrollers, and the time unit for the recorded execution time is a microsecond. Since the model execution time is equal to 2 ms in the model simulator, the control signals must be computed on the processor before the next sequence. Therefore the loop requirement for the implemented PIL is two milliseconds. Both the Discovery board and Arduino Mega pass the loop requirement, while STM32F407 shows better performance.

6. Conclusions and future studies

In this paper, an adaptive haptic shared control paradigm is modeled wherein the human and automation system each is modeled as an agent with a two-level hierarchical control approach. To allow the co-robot to dynamically and continuously negotiate the driver's control authority, we developed a stochastic optimal control approach. Specifically, we employed a nonlinear model predictive approach subjected to probabilistic uncertainties in humans biomechanics to solve the optimal control problem and used the continuation generalized minimum residual method to solve the nonlinear cost function. The polynomial chaos expansions are employed to propagate the probabilistic stiffness/damping uncertainties through the system model for obtaining a computationally tractable form of the optimal problem. A series of numerical simulations are conducted to demonstrate the adaptive haptic shared control paradigm's effectiveness in negotiating the control authority. Our simulations involved two conditions when the control authority shifts from the human to the automation system (active safety mode), as well as when the control authority shifts from the automation system to human (assistive mode). Also, we included two scenarios where the human and automation are in cooperative and uncooperative mode. Furthermore, to ensure that the developed modulation algorithms can be implemented in a human-in-the-loop setup, we performed a series of processors in the loop experiments using a low-cost set of microcontrollers.

A set of challenges needs to be addressed prior to implementing the proposed shared control paradigm in real-world applications. These challenges are the subjects of our future studies. In particular, in this paper, it is assumed that the human partner's bio-mechanics parameters and intent are known. In the future, we plan to develop an online learning approach to estimate these parameters and track them in real-time as they vary. Furthermore, we plan to create a method that allows recognizing the current interaction mode in real-time using the data acquired by on-board sensors. By knowing the interaction mode, an appropriate cost function can be defined, and the automation system can adjust its behavior based on this cost function. Furthermore, while the main focus of this paper was to develop an adaptive impedance controller, knowing how fast the transition should be applied is another challenge. In this paper, we arbitrarily set the parameters of α_A and β_A.

However, it is essential to test various transition schemes, including discrete and slow or fast continuous transitions, to determine an optimal speed for exchanging the control authority. Finally, the developed models shall be tested and refined in a hardware-in-the-loop test-bed.

CRediT authorship contribution statement

Vahid Izadi: Writing - original draft, Conceptualization, Methodology, Controller design, Simulation/PIL implementation. **Amir H. Ghasemi:** Supervision, Writing - review & editing.

Declaration of competing interest

The authors declare that they have no known competing financial interests or personal relationships that could have appeared to influence the work reported in this paper.

References

[1] Ghasemi AH, Jayakumar P, Gillespie RB. Shared control architectures for vehicle steering. Cognit Technol Work 2019;1–11.

[2] Bhardwaj A, Ghasemi AH, Zheng Y, Febbo H, Jayakumar P, Ersal T, et al. Who's the boss? Arbitrating control authority between a human driver and automation system. Transp Res F 2020;68:144–60.

[3] Agah A. Human interactions with intelligent systems: research taxonomy. Comput Electr Eng 2000;27(1):71–107.

[4] Albu-Schaffer A, Bicchi A, Boccadamo G, Chatila R, De Luca A, De Santis A, et al. Physical human-robot interaction in anthropic domains: safety and dependability. In: Proceeding 4th IARP/IEEE-EURON workshop on technical challenges for dependable robots in human environments. 2005.

[5] Beyl P, Knaepen K, Duerinck S, Van Damme M, Vanderborght B, Meeusen R, et al. Safe and compliant guidance by a powered knee exoskeleton for robot-assisted rehabilitation of gait. Adv Robot 2011;25(5):513–35.

[6] Boehm P, Ghasemi AH, O'Modhrain S, Jayakumar P, Gillespie RB. Architectures for shared control of vehicle steering. IFAC-PapersOnLine 2016;49(19):639–44.

[7] Ghasemi AH, Johns M, Garber B, Boehm P, Jayakumar P, Ju W, et al. Role negotiation in a haptic shared control framework. In: Adjunct proceedings of the 8th international conference on automotive user interfaces and interactive vehicular applications. ACM; 2016, p. 179–84.

[8] Ghasemi AH, Rastgoftar H. Adaptive haptic shared control framework using Markov decision process. In: Dynamic systems and control conference (DSCC), 2018. ASME; 2018.

[9] Ghasemi AH. Game theoretic modeling of a steering operation in a haptic shared control framework. In: Dynamic systems and control conference (DSCC), 2018. ASME; 2018.

[10] Vitiello N, Lenzi T, Roccella S, De Rossi SMM, Cattin E, Giovacchini F, et al. Neuroexos: A powered elbow exoskeleton for physical rehabilitation. IEEE Trans Robot 2013;29(1):220–35.

[11] Izadi V, Yeravdekar A, Ghasemi A. Determination of roles and interaction modes in a haptic shared control framework. In: ASME 2019 dynamic systems and control conference. American Society of Mechanical Engineers Digital Collection; 2019.

[12] Peternel L, Tsagarakis N, Caldwell D, Ajoudani A. Robot adaptation to human physical fatigue in human–robot co-manipulation. Auton Robots 2018;42(5):1011–21.

[13] Au S, Berniker M, Herr H. Powered ankle-foot prosthesis to assist level-ground and stair-descent gaits. Neural Netw 2008;21(4):654–66.

[14] Townsend EC, Mielke EA, Wingate D, Killpack MD. Estimating human intent for physical human-robot co-manipulation. 2017, ArXiv Preprint arXiv:1705.10851.

[15] Yu B, Gillespie RB, Freudenberg JS, Cook JA. Identification of human feedforward control in grasp and twist tasks. In: American control conference (ACC), 2014. IEEE; 2014, p. 2833–8.

[16] Cole DJ. Neuromuscular dynamics and steering feel. Tech. rep., Proc. Steering Tech; 2008.

[17] Wang Z, Peer A, Buss M. An HMM approach to realistic haptic human-robot interaction. In: World haptics 2009-third joint eurohaptics conference and symposium on haptic interfaces for virtual environment and teleoperator systems. IEEE; 2009, p. 374–9.

[18] Schrempf OC, Hanebeck UD, Schmid AJ, Worn H. A novel approach to proactive human-robot cooperation. In: ROMAN 2005. IEEE international workshop on robot and human interactive communication, 2005. IEEE; 2005, p. 555–60.

[19] Agravante DJ, Cherubini A, Bussy A, Gergondet P, Kheddar A. Collaborative human-humanoid carrying using vision and haptic sensing. In: 2014 IEEE international conference on robotics and automation (ICRA). IEEE; 2014, p. 607–12.

[20] Madan CE, Kucukyilmaz A, Sezgin TM, Basdogan C. Recognition of haptic interaction patterns in dyadic joint object manipulation. IEEE Trans Haptics 2014;8(1):54–66.

[21] Kucukyilmaz A, Issak I. Online identification of interaction behaviors from haptic data during collaborative object transfer. IEEE Robot Autom Lett 2019;5(1):96–102.

[22] Oguz SO, Kucukyilmaz A, Sezgin TM, Basdogan C. Haptic negotiation and role exchange for collaboration in virtual environments. In: Haptics symposium, 2010 IEEE. IEEE; 2010, p. 371–8.

[23] Oguz SO, Kucukyilmaz A, Sezgin TM, Basdogan C. Supporting negotiation behavior with haptics-enabled human-computer interfaces. IEEE Trans Haptics 2012;5(3):274–84.

[24] Stefanov N, Peer A, Buss M. Online intention recognition for computer-assisted teleoperation. In: Robotics and automation (ICRA), 2010 IEEE international conference on. IEEE; 2010, p. 5334–9.

[25] Stefanov N, Peer A, Buss M. Role determination in human-human interaction. In: EuroHaptics conference, 2009 and symposium on haptic interfaces for virtual environment and teleoperator systems. world haptics 2009. third joint. IEEE; 2009, p. 51–6.

[26] Jamieson GA, Vicente KJ. Designing effective human-automation-plant interfaces: A control-theoretic perspective. Human Fact 2005;47(1):12–34.

[27] Kim K, Colgate JE. Haptic feedback enhances grip force control of sEMG-controlled prosthetic hands in targeted reinnervation amputees. IEEE Trans Neural Syst Rehabil Eng 2012;20(6):798–805.

[28] Sergi F, Accoto D, Campolo D, Guglielmelli E. Forearm orientation guidance with a vibrotactile feedback bracelet: On the directionality of tactile motor communication. In: 2008 2nd IEEE RAS & EMBS international conference on biomedical robotics and biomechatronics. IEEE; 2008, p. 433–8.

[29] Christiansen R, Contreras-Vidal JL, Gillespie RB, Shewokis PA, O'Malley MK. Vibrotactile feedback of pose error enhances myoelectric control of a prosthetic hand. In: 2013 world haptics conference (WHC). IEEE; 2013, p. 531–6.

[30] Boehm P, Ghasemi A, O'Modhrain S, Jayakumar P, Gillespie R. Architectures for shared control of vehicle steering. In: IFAC - human and machine symposium. 2016.

[31] Mesbah A, Streif S, Findeisen R, Braatz RD. Stochastic nonlinear model predictive control with probabilistic constraints. In: 2014 american control conference. IEEE; 2014, p. 2413–9.

[32] Oldewurtel F, Sturzenegger D, Esfahani PM, Andersson G, Morari M, Lygeros J. Adaptively constrained stochastic model predictive control for closed-loop constraint satisfaction. In: 2013 american control conference. IEEE; 2013, p. 4674–81.

[33] Mori H, Seki K. Continuation Newton-GMRES power flow with linear and nonlinear predictors. In: 2007 large engineering systems conference on power engineering. IEEE; 2007, p. 171–5.

[34] Soneda Y, Ohtsuka T. Nonlinear moving horizon state estimation with continuation/generalized minimum residual method. J Guid Control Dyn 2005;28(5):878–84.

[35] Ohtsuka T, Fujii H. Stabilized continuation method for solving optimal control problems. J Guid Control Dyn 1994;17(5):950–7.

[36] Ohtsuka T. Continuation/GMRES method for fast algorithm of nonlinear receding horizon control. In: Proceedings of the 39th IEEE conference on decision and control (Cat. No. 00CH37187). Vol. 1, IEEE; 2000, p. 766–71.

[37] Kelley CT. Iterative methods for linear and nonlinear equations. Vol. 16, Siam; 1995.

[38] Ohtsuka T. A continuation/GMRES method for fast computation of nonlinear receding horizon control. Automatica 2004;40(4):563–74.

[39] Bhardwaj A, Gillespie B, Freudenberg J. Estimating rack force due to road slopes for electric power steering systems. In: 2019 american control conference (ACC). IEEE; 2019, p. 328–34.

[40] Zhao Y, Chevrel P, Claveau F, Mars F. Continuous identification of driver model parameters via the unscented Kalman filter. IFAC-PapersOnLine 2019;52(28):126–33.

[41] Yu B, Gillespie RB, Freudenberg JS, Cook JA. Human control strategies in pursuit tracking with a disturbance input. In: Decision and control (CDC), 2014 IEEE 53rd annual conference on. IEEE; 2014, p. 3795–800.

[42] Wiener N. The homogeneous chaos. Amer J Math 1938;60(4):897–936.

[43] Ghanem RG, Spanos PD. Stochastic finite elements: A spectral approach. Courier Corporation; 2003.

[44] Smith RC. Uncertainty quantification: theory, implementation, and applications. Vol. 12, Siam; 2013.

[45] Fagiano L, Khammash M. Nonlinear stochastic model predictive control via regularized polynomial chaos expansions. In: 2012 IEEE 51st IEEE conference on decision and control (CDC). IEEE; 2012, p. 142–7.
[46] Tapia RA. Role of slack variables in quasi-newton methods for constrained optimization. Tech. rep., Rice Univ., Houston, TX (USA). Dept. of Mathematical Sciences; 1979.
[47] Bryson AE. Applied optimal control: optimization, estimation and control. CRC Press; 1975.
[48] Melendez-Calderon A, Komisar V, Ganesh G, Burdet E. Classification of strategies for disturbance attenuation in human-human collaborative tasks. In: 2011 annual international conference of the IEEE engineering in medicine and biology society. IEEE; 2011, p. 2364–7.
[49] Jarrassé N, Charalambous T, Burdet E. A framework to describe, analyze and generate interactive motor behaviors. PLoS One 2012;7(11).
[50] Hasser CJ, Cutkosky MR.
[51] Ghasemi A, Yeravdekar A. Modelling non cooperative human-automation interactions in a haptic shared control framework. Tech. rep., SAE Technical Paper; 2019.
[52] Paulson JA, Mesbah A. An efficient method for stochastic optimal control with joint chance constraints for nonlinear systems. Internat J Robust Nonlinear Control 2019;29(15):5017–37.

Vahid Izadi received a B.S. degree in Electrical Engineering and Electronics from Hamedan University of Technology in 2012, an M.S. degree in Electrical Engineering and Electronics from Iran University of Science and Technology and is currently a Ph.D. Student at the Department of Mechanical Engineering and Engineering Science at the University of North Carolina at Charlotte.

Amirhossein Ghasemi received a B.S. degree in Mechanical Engineering from the Ferdowsi University of Mashhad in 2005, an M.S. degree in Mechanical Engineering from Amirkabir University in 2008, and the Ph.D. degree in Mechanical Engineering from the University of Kentucky in 2012. He is currently an Assistant Professor in the Department of Mechanical Engineering and Engineering Science at the University of North Carolina at Charlotte.